Combining Electrical Resistivity, Induced Polarization, and Self-Potential for a Better Detection of Ore Bodies

Zhaoyang Su, André Revil, Ahmad Ghorbani, Xin Zhang, Xiang Zhao, Jessy Richard

minerals

MDPI

Article

Combining Electrical Resistivity, Induced Polarization, and Self-Potential for a Better Detection of Ore Bodies

Zhaoyang Su [1,2], André Revil [2,*], Ahmad Ghorbani [3], Xin Zhang [4], Xiang Zhao [5] and Jessy Richard [3]

[1] State Key Laboratory of Petroleum Resources and Prospecting, China University of Petroleum, Beijing 102249, China; 2019310419@student.cup.edu.cn
[2] Université Grenoble Alpes, Université Savoie Mont-Blanc, CNRS, UMR CNRS 5204, EDYTEM, 73370 Le Bourget du Lac, France
[3] Naga Geophysics, Technolac, 73370 Le Bourget du Lac, France
[4] School of Safety Engineering, China University of Mining and Technology, Xuzhou 221116, China
[5] School of Earth Science and Engineering, Hohai University, Nanjing 211100, China
* Correspondence: andre.revil@univ-smb.fr

Abstract: Electrical resistivity (ER), induced polarization (IP), and self-potential (SP) are three geophysical methods that have been broadly used in the realm of mineral exploration. These geophysical methods provide complementary information, each exhibiting a distinct sensitivity to various types of mineral deposits. Considering the relationship among these three methods, we propose an integrated approach that merges their respective information to offer an improved localization technique for ore bodies. First, we invert the electrical conductivity distribution through electrical resistance tomography (ERT). Then, we use the inverted conductivity distribution to invert the IP and SP data in terms of chargeability and source current density distributions. Then, we normalize the inverted chargeability and source current density distributions and we combine them to obtain an ore body index (ORI) χ used to delineate the potential locations of ore deposits. We design this index to be sensitive to the presence of ore bodies, which are reflected by either strong and localized source current density (SP) and/or strong chargeability values (IP). The proposed method is first validated using a synthetic model with two distinct anomalies characterized by different properties. The results show the limitation of individual inversion, as each method exclusively detects one of these anomalies. The combined approach allows a better characterization of the target. Then, the approach is applied to a sandbox experiment in which two metallic bodies are buried in water-saturated sand used as the background. Again, the proposed methodology is successfully applied to the detection of the metallic targets, improving their localization compared with individual methods.

Keywords: electrical resistivity tomography (ERT); induced polarization (IP); self-potential (SP); ore body index (ORI); exploration of mineral resources

Citation: Su, Z.; Revil, A.; Ghorbani, A.; Zhang, X.; Zhao, X.; Richard, J. Combining Electrical Resistivity, Induced Polarization, and Self-Potential for a Better Detection of Ore Bodies. *Minerals* **2024**, *14*, 12. https://doi.org/10.3390/min14010012

Academic Editor: Emilio L. Pueyo

Received: 7 November 2023
Revised: 18 December 2023
Accepted: 19 December 2023
Published: 20 December 2023

1. Introduction

The global demand for minerals is on the rise due to population growth, urbanization, and industrialization, but the exploration for new mineral resources is becoming increasingly challenging since large and shallow targets are mostly exhausted [1]. The successful rate of discovering new ore deposits has consistently declined over time in recent decades [2]. This decline can be attributed to several factors, such as thick overlying soil layers; remote and secluded geographical regions; a decrease in the quality of ore grades; as well as social and environmental impacts, among other reasons [1].

Exploration technology has made tremendous advances in the past 30 years [3]. Geophysical methods such as the seismic [4,5], airborne electromagnetic [6–9], gravity [10–12], and magnetic methods [13–15] have played a crucial role in uncovering concealed deposits that are geologically challenging to identify. In particular, low-frequency geoelectrical methods like the electrical resistivity (ER), the induced polarization (IP), and the self-potential

(SP) geophysical methods are non-invasive and cost-efficient in the realm of mineral exploration. These geophysical findings also can be effectively integrated into the overall geological and geochemical conceptual model [16].

ER is a method used to determine the subsurface resistivity/conductivity distribution of the study area. The electrical conductivity describes the ability of a material to allow the flow of current. Electrical conductivity is sensitive to various parameters like fluid contents, pore water salinity, and clay and ore contents [17]. Consequently, ER has been extensively used in hydrogeophysics [18,19], mining [20,21], geotechnical investigations [22], and environmental surveys [17,23]. It is often though that ore bodies are usually characterized by high conductivities and could be easily detected by the ER method [24–27]. However, due to the complex geological conditions of certain ore deposits and the presence of ore minerals in the form of very small particles or dispersed forms within the host rocks, the resistivity contrast between these ore bodies and the surrounding rocks is not always high. Furthermore, ore bodies may appear as insulators at low frequencies because of their polarization [28–31]. As a result, ERT alone cannot be used to assess the position of ore bodies [30].

The IP method was first described by [32] and has been broadly used in the exploration of ore bodies [1]. Metallic bodies can be polarized under the primary current and electric field [28,33]. IP is therefore a powerful tool able to locate mineral deposits [34–39]. The recently developed petrophysical model for IP of metallic ore immersed in a porous conductive and polarizable material showed that chargeability of the material is linearly dependent on the volume fraction of metallic ore and the chargeability of the surrounding background material [28,33]. IP is sensitivity to ore deposits containing disseminated metallic particles (pyrite, magnetite), but clay-rich materials and graphite can also generate strong polarizations, potentially misleading the interpretation of IP data if used as a stand-alone technique [1].

The SP method is a passive geoelectrical method [40]. The electrical potential distribution at the surface of a geological object is mapped. The resulting electrical potential map is then interpreted in terms of causative source current distribution in the subsurface. In essence, the method is similar to electroencephalography (EEG) in medical imaging [41,42], and the same underlying Poisson equation is solved [40]. In EEG, the source current density is related to the opening of ionic channels at the synapses between neurons generating electromagnetic signals. The record of the resulting electrical potential distribution is made at the scalp [43] and the head is considered as a conductive body. In geophysics, the source current density is mostly associated with the flow of the ground water through an electrokinetic coupling effect called the streaming potential [44]. Another source is related to the presence of ore bodies in a conductive background crossed by a gradient in the redox potential [45]. This second case is similar to a car battery generating its own current density. Both in EEG and in geophysics, the goal is to invert the recorded electrical potential signals in order to characterize the causative current source accounting for the electrical conductivity distribution, which modulates the electrical potential response between the source and the recording stations.

ER, IP, and SP methods provide complementary information, with each method exhibiting a distinct sensitivity to various types of mineral deposits. In the past, several authors have qualitatively underlined how some of these methods can be combined with another one for mineral exploration and hydrogeology. For instance, integrating ERT, IP, and SP methods to qualitatively evaluate a graphitic body [46] and gold mineralization [47]. The authors of [48] integrate these three methods to evaluate the subsurface and its engineering suitability for construction. The authors of [49] simultaneously collected SP and ER data for the detection of seafloor massive sulfide deposits. They usually use the collected 2D SP data to outline the ore at the surface and obtained the depth information from inverted 2D/3D conductivity or chargeability distribution. Marine SP tomography has been recently used to image seafloor massive sulfide deposits [50–52]. However, to perform SP inversion, we require the conductivity distribution below the surface (or seafloor) [40,53]. In addition,

single geophysical inversion often exhibits non-uniqueness due to the uncertainty in the observed data [54]. Therefore, the quantitative integration of ER, IP, and SP surveys becomes imperative in this scenario, enabling a more comprehensive characterization of ore bodies.

In this paper, our primary objective is to develop a quantitative approach integrating ERT, IP, and SP methods to enhance the 3D localization of ore deposits. This is achieved by defining an ore body index (ORI). We first present a concise overview of the methodology and inversion techniques of these methods. Subsequently, we apply our newly defined index on a 3D synthetic model and then on a sandbox experiment. The results of our combined interpretation demonstrate a clear advantage over individual inversion.

2. Methodology

2.1. Self-Potential Method

Negative SP anomalies (sometimes amounting on the shore to several hundreds of millivolts) are associated with redox-active environments in which metallic bodies are located [40,45]. As a passive method, we just need two non-polarization electrodes and a high-impedance voltmeter to perform an SP survey [40]. The method is therefore cheap and easy to carry out in field conditions.

Total current density $\mathbf{J}_{tol}$ is the sum of Ohm's law (associated with the transport of electrical charges by conduction) and a source current density [55],

$$\mathbf{J}_{tol} = \sigma\mathbf{E} + \mathbf{J}_s \tag{1}$$

where σ(S/m) denotes the electrical conductivity below the surface, $\mathbf{E} = -\nabla\psi$ is the quasi-static electrical field, and ψ is the electric potential (or SP) distribution. Using the conservation of charge in the low-frequency limit of Maxwell equations $\nabla \cdot \mathbf{J} = 0$, we obtain the following governing field equation for the SP method [40,56]:

$$\nabla \cdot (\sigma\nabla\psi) = \nabla \cdot \mathbf{J}_s = q_v \tag{2}$$

where ψ(V) denotes the electrical potential (in V), the $\mathbf{J}_s$ (A/m^2) is surface current density, q_v (A/m^3) is the equivalent charge density per unit volume corresponding to the source. The direct multifrontal massively parallel sparse direct solver (MUMPS) is used to solve Equation (2) [57,58]. We can rewrite the above Equation (2) [59–61]:

$$\nabla^2\psi = \frac{q_v}{\sigma} + \nabla \ln\sigma \cdot \mathbf{E} \tag{3}$$

From Equation (3) (from Equations (2) to (3), see Appendix A), we notice that the subsurface conductivity distribution σ influences the observed SP data [62]. Moreover, this conductivity distribution is used to calculate the kernel matrix of the SP problem (the calculation of the kernel matrix is described in [60]). Therefore, it is important when using the electrical conductivity distribution from the ERT in SP inversion to calculate the source current distribution [53,59]. Nonetheless, when conducting SP inversion independently, it is common practice to assume a homogeneous conductivity distribution. However, a more favorable approach is to incorporate the conductivity distribution obtained from ERT or transient electromagnetic (TEM) inversion results if available. This enhances the accuracy of the SP inversion in separating ghosts (associated with electrical conductivity contrasts) from true sources associated with ore bodies [59,60].

In the realm of deterministic inversion, SP tomography is a linear problem. Given the value of the regularization parameter, the solution is therefore obtained in a single iteration. However, the optimization of the regularization parameter itself (for instance, through the use of the L-curve technique) implies a set of iterations to obtain an optimized solution. The most important thing is that we should add the depth weight in the SP inversion. Additionally, we also use the minimum support (MS) method to reconstruct a compact

volumetric source current density. The general form of the objective function is to combine the data fitting term and the model constraint term [40]:

$$\varphi^{\beta}(\mathbf{m}_{\mathrm{w}}^{\mathrm{q}}) = \left\|\mathbf{W}_d(\mathbf{K}_w\mathbf{m}_{\mathrm{w}}^{\mathrm{q}} - \mathbf{d}_{\mathrm{obs}})\right\|_2^2 + \beta\left\|\mathbf{W}_m(\mathbf{m}_{\mathrm{w}}^{\mathrm{q}} - \mathbf{m}_{\mathrm{ref}}^{\mathrm{q}})\right\|_2^2 \tag{4}$$

where the $\mathbf{W}_d$ is the diagonal data-weighting matrix, $\mathbf{W}_m$ is the roughness operator used here to obtain a smooth inversion result, $\mathbf{d}_{\mathrm{obs}}$ is the observed data, $\mathbf{m}_{\mathrm{ref}}^{\mathrm{q}}$ is the reference model, and $\mathbf{m}_{\mathrm{w}}^{\mathrm{q}}$ is the optimized (inverted) model. The regularization parameter (trade-off) β is used to balance the data misfit term (first term in Equation (4)) and the model constraint term (second term in Equation (4)). The value β is determined by a cooling strategy in this paper, while other methods include the L-curve criterion [63]. The depth-weighting matrix is based on the sensitivity matrix and defined as

$$\mathbf{\Lambda} = \mathrm{diag}(\sum_{i=1}^{N} K_{ij}^2)^{\frac{1}{4}} \tag{5}$$

where K_{ij} is the element of the raw kernel matrix $\mathbf{K}$, and N is the number of SP data. With the minimum support (MS) function [64], the diagonal weighting matrix $\mathbf{\Pi}$ is defined as [65]

$$\mathbf{\Pi} = \mathrm{diag}\left(\sqrt{\frac{\Lambda_{kk}^2}{m_{k-1}^2 + \alpha^2}}\right) \tag{6}$$

where Λ_{kk} is the elements of the diagonal depth-weighting matrix, m_{k-1} is the model at the last iteration (k $-$ 1), and α is a small threshold value [65]. The new kernel matrix is $\mathbf{K}_w = \mathbf{K}\mathbf{\Pi}^{-1}$. The solution $\mathbf{m}_{\mathrm{w}}^{\mathrm{q}}$ of Equation (4) is a sensitivity-scaled solution. According to $\mathbf{m}^* = \mathbf{\Pi}^{-1}\mathbf{m}_{\mathrm{w}}^{\mathrm{q}}$, the depth-weighting volumetric source current density distribution $\mathbf{m}^*$ will be obtained.

2.2. Electrical Resistivity Tomography

ER is an active method and the electrode array includes two current electrodes (inject electrode A and retrieve electrode B) and two voltage electrodes (M and N). The acquired voltage different φ between M and N and input currents I are related to the subsurface conductivity distribution satisfying the following Poisson's field equation [66]:

$$\nabla \cdot (\sigma_\infty \nabla \varphi_{\sigma_\infty}) = -I(\delta(r - r_{s+}) - \delta(r - r_{s-})) \tag{7}$$

where σ_∞ (in S/m) denotes the instantaneous conductivity (without polarization effect) in Figure 1, φ_{σ_∞} (in V) is electrical potential field generated by the injection/retrieval of the current I (in A), $\delta(r - r_s)$ is the Dirac delta function, r_{s+} and r_{s-} are the locations of the positive (electrode A) and negative current sources (electrode B), respectively. Neumann boundary conditions were used at the Earth's surface.

Different from the SP inversion, ERT is a non-linear optimization problem. The objective function is as follows:

$$\phi^{\beta}(\mathbf{m}) = \|\mathbf{W}_d(f(\mathbf{m}) - \mathbf{d}_{\mathrm{obs}})\|_2^2 + \beta\|\mathbf{W}_m(\mathbf{m} - \mathbf{m}_{\mathrm{ref}})\|_2^2 \tag{8}$$

where $\mathbf{d}_{\mathrm{obs}}$ is the vector of observed data (ψ_{σ_∞}) and $f(\mathbf{m})$ is the vector of predicted data, $\mathbf{m}_{\mathrm{ref}}$ is the reference model. $\mathbf{m}$ is the model that we want to estimate (here, the model parameters are $\ln(\sigma)$).

The solution $\mathbf{m}_n$ corresponds to the minimum of the objective function (8) at the n_{th} iteration, so we need to calculate the gradient of Equation (8),

$$\mathbf{g}_n = 2\mathbf{J}^T\mathbf{W}_d^T\mathbf{W}_d\mathbf{r}_{n-1} + 2\beta\mathbf{W}_m^T\mathbf{W}_m(\mathbf{m}_{n-1} - \mathbf{m}_{\mathrm{ref}}) \tag{9}$$

where $\mathbf{r}_{n-1} = f(\mathbf{m}_{n-1}) - \mathbf{d}_{\text{obs}}$ is the difference in predicted data and observed data, and Jacobian (sensitivity) matrix $\mathbf{J}$ is defined as

$$\mathbf{J} = \frac{\partial f(\mathbf{m}_{n-1})}{\partial m} \tag{10}$$

Performing the Taylor series expansion of the function $f(\mathbf{m})$ at the $\mathbf{m}_n$ and neglecting the second-order term and higher-order terms, $f(\mathbf{m}_{n-1}) = f(\mathbf{m}_n) - \mathbf{J}\delta\mathbf{m}_n$ and setting the gradient $\mathbf{g}_n = 0$, Equation (9) can be written as

$$(\mathbf{J}^T\mathbf{W}_d^T\mathbf{W}_d\mathbf{J} + \beta\mathbf{W}_m^T\mathbf{W}_m)\delta\mathbf{m} = -\mathbf{J}^T\mathbf{W}_d^T\mathbf{W}_d\mathbf{r}_n - \beta\mathbf{W}_m^T\mathbf{W}_m(\mathbf{m}_n - \mathbf{m}_{\mathbf{ref}}) \tag{11}$$

The preconditioner conjugate gradient (PCG) solver is used to approximately solve Equation (9) and then update the model according to

$$\mathbf{m}_{n+1} = \mathbf{m}_n + \mu\delta\mathbf{m} \tag{12}$$

where $\mathbf{m}_{n+1}$ is the updated model and the $\mathbf{m}_n$ is the solution of the current iteration. μ is a simple line-search parameter, making sure the new model update adequately reduces the objective function (8) [67].

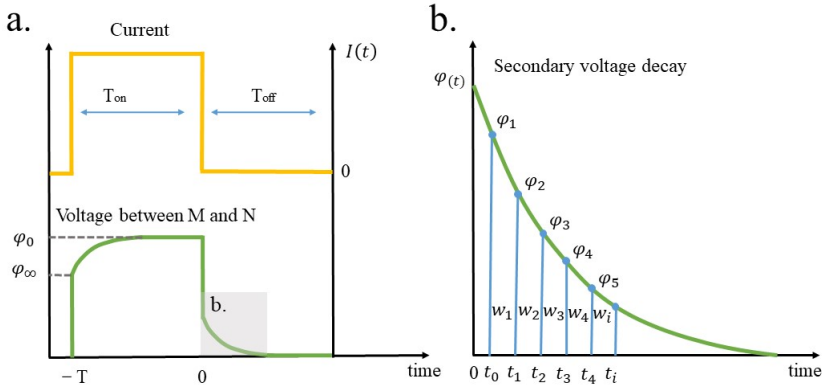

Figure 1. Time-domain-induced polarization. (**a**) The yellow curve denotes the current injection I, the green denotes the voltage difference φ from the measurement electrodes M and N. (**b**) Secondary voltage $\varphi(t)$ decay curve, the partial chargeability $M(t_i, t_{i+1})$ is obtained by integrating the response over each window (w_1, w_2, etc.).

2.3. Induced Polarization Method

Figure 1 illustrates the concept of time-domain-induced polarization (TDIP). In TDIP, the process of polarization is characterized by a dimensionless property called the "chargeability", and the chargeability M is defined as [28,33]

$$M = \frac{\sigma_\infty - \sigma_0}{\sigma_\infty}, \tag{13}$$

where σ_0 denotes the direct current (DC) conductivity. If we know the chargeability M and inverted instantaneous conductivity σ_∞ from ERT, we can obtain the apparent chargeability by forward modelling twice using Equation (7). According to Equation (13), we substitute DC conductivity σ_0 for σ_∞ in Equation (7), and the potential field distribution φ_{σ_0} can be obtained by re-running the forward modelling step for the DC condition,

$$\nabla \cdot (\sigma_\infty(1 - M)\nabla\varphi_{\sigma_0}) = -I(\delta(r - r_{s+}) - \delta(r - r_{s-})) \tag{14}$$

The observed data (apparent chargeability) M_a (dimensionless) in the TDIP survey are related to the initial voltage φ_{σ_∞} and the steady-state or DC voltage φ_{σ_0} and can be calculated [31],

$$M_a = \frac{\varphi_{\sigma_0} - \varphi_{\sigma_\infty}}{\varphi_{\sigma_0}} \tag{15}$$

In the IP survey, we usually record the partial chargeability. The secondary voltage is measured with windows after the primary current is shut down (Figure 1b). These data are utilized to determine the apparent chargeability. In order to minimize electrodes' polarization effects, we design the current electrode pair [A B] at the boundary, and the measure electrode pair [M N] is inside. The secondary voltage is monitored using integrated windows to have a high signal-to-noise ratio. For measuring window w_i between t_i and t_{i+1}, the partial chargeability is calculated as follows:

$$M_{t_1,t_2} = \frac{1}{\varphi_0}\int_{t_1}^{t_2} \varphi(t)dt \tag{16}$$

where M_{t_1,t_2} is recorded partial chargeability by the IP system (in mV/V), and the apparent chargeability M_a used in inversion can be calculated using the mean value theorem,

$$M_{t_1,t_2} = M_a(t_2 - t_1) \tag{17}$$

here, $t_1 < t_2 << \tau$ guarantee the linear relationship [35], and τ is the time constant. The secondary voltage $\varphi(t)$ is measured in windows (w_1, w_2, etc.) separated by time (t_0, t_1, ...) (Figure 1b). The time windows are set to equal ($t_i - t_{i-1} = 0.1$ s) in this IP survey, and in total 10 partial chargeability M_{t_1,t_2} (mV/V) values were determined. So, the $M_a = M_{t_1,t_2}/100$ (V/V). There are two ways to invert the IP data. One is using the average apparent chargeability of all the windows [68], and the other is using the apparent chargeability calculated from the first integral window which would be better to estimate the intrinsic chargeability [69] because it is closer to the true response of the decay curve (secondary voltage over primary voltage at the time when the current is shut down). Here, we chose the second method to invert IP data.

In this section, we introduce how to calculate sensitivity matrix $\mathbf{J}_{IP}$ (the sensitivity of apparent chargeability M_a with respect to the intrinsic chargeability M). The matrix $\mathbf{J}_{IP}$ is defined as

$$\mathbf{J}_{IP} = \frac{\partial M_a}{\partial M} \tag{18}$$

According to Equation (15), Equation (18) can be rewritten as

$$\mathbf{J}_{IP} = \frac{\partial\left(\frac{\varphi_{\sigma_0} - \varphi_{\sigma_\infty}}{\varphi_{\sigma_0}}\right)}{\partial M}, \tag{19}$$

$$\mathbf{J}_{IP} = \frac{\varphi_{\sigma_\infty}}{(\varphi_{\sigma_0})^2}\frac{\partial \varphi_{\sigma_0}}{\partial M}. \tag{20}$$

According to the chain rule of derivation

$$\frac{\partial \varphi_{\sigma_0}}{\partial \sigma_0} = \frac{\partial \varphi_{\sigma_0}}{\partial M}\cdot\frac{\partial M}{\partial \sigma_0} = -\frac{1}{\sigma_\infty}\frac{\partial \varphi_{\sigma_0}}{\partial M} \tag{21}$$

So, combining Equations (20) and (21), Equation (18) can finally be written as

$$\mathbf{J}_{IP} = -\sigma_\infty \cdot \frac{\varphi_{\sigma_\infty}}{(\varphi_{\sigma_0})^2}\frac{\partial \varphi_{\sigma_0}}{\partial \sigma_0} = -\frac{\sigma_\infty}{\sigma_0}\cdot\frac{\varphi_{\sigma_\infty}}{(\varphi_{\sigma_0})^2}\frac{\partial \varphi_{\sigma_0}}{\partial \ln \sigma_0} \tag{22}$$

The chargeability sensitivity matrix $\mathbf{J}_{IP}$ has a relationship with the conductivity sensitivity matrix $\mathbf{J}_{DC}$, so, the code developed for inverting DC data requires minor changes to invert IP data [70]. We do not need to explicitly compute the sensitivity matrix $\mathbf{J}_{DC}$ in

the ERT. Instead, we compute the matrix–vector product of $\mathbf{J}_{DC}\mathbf{v}$, which is equivalent in solving the adjoint forward problem [67]. If we want to join IP and SP data inversion, we should explicitly compute the chargeability sensitivity matrix $\mathbf{J}_{IP}$ and the current density sensitivity matrix $\mathbf{J}_{SP}$. Actually, we firstly compute the sensitivity matrix $\mathbf{J}_{DC}$ of ERT,

$$\mathbf{J}_{DC} = \frac{\partial \varphi_{\sigma_0}}{\partial \ln(\sigma_0)} \tag{23}$$

then we use Equation (23) to explicitly calculate the matrix $\mathbf{J}_{IP}$.

2.4. The Integrated Analysis of IP and SP Results

Here, our aim is to combine the inverted chargeability and source current density from the traditional IP and SP surveys to delineate the ore deposits. The inverted chargeability and current density were normalized using the following linear transformation to normalize the values of both data to 0–1:

$$m_{norm} = \frac{m - m_{\min}}{m_{\max} - m_{\min}}, \tag{24}$$

where m denotes the raw inverted model, $m_{\max}$ and $m_{\min}$ represent the maximum and minimum value of m, respectively. Here we define an ore body index (ORI) χ (dimensionless) that is sensitive to the presence of the ore body. The ORI distribution is calculated by using the sum of the ORI for IP and SP, in which ERT has been used to better determine the true sources associated with ore bodies:

$$\chi = m_{norm}^{IP} + m_{norm}^{SP}. \tag{25}$$

We notice that the two kinds of data use equal weighting if the anomaly also showed high chargeability and source current density, and the ORI χ is close to 2; if the anomaly only has one character (chargeability or current density), the ORI $\chi \approx 1$. Because we use the L2 norm in the inversion, the inverted model will be smooth, and we define a threshold greater than 0.5 to delineate the ore body.

3. Synthetic Test

Here, we design a 3D synthetic model, whose size is similar to the sandbox. Considering the difficult conditions currently facing mineral resource exploration, two different anomalies with different sizes are located at the center of the box. The first anomaly (C1) is buried beneath the surface, whose size is 0.1 m × 0.1 m × 0.1 m, with a low conductivity of 0.3 S/m, a high chargeability of 0.2, and a volume current density of 0 mA/m^3. The second anomaly (C2) is a vertical, slender metal bar from the surface to the bottom (C2), whose size is 0.05 m × 0.05 m × 0.20 m, with a high conductivity of 10 S/m, a low chargeability of 0.1, and a volume current density of 2.5 mA/m^3. The background conductivity is 0.025 S/m, and the chargeability and current density are 0. For the synthetic tests, we use the same protocol as the sandbox experiment below. In total, 64 positions were used to inject current and acquisition voltage potential difference. The space of the electrode is 6 cm (y direction) and 4 cm (x direction). For ERT and IP, in total there are 237 potential fields and apparent chargeability. For SP, 64 voltage differences were recorded.

3.1. ERT

The model was a meshed 40 × 40 × 25 grid, and each cell is 0.02 m × 0.02 m × 0.02 m (Figure 2). Neumann boundary conditions are used at all the boundaries. Conductivity tomography is finished after 5 iterations (Figure 3). ERT is sensitive to ore bodies with significant conductivity differences from the host rock, so, the anomaly C2 is better imaged than anomaly C1, but the worse resolution of the boundary could be attributed to the ore body's small size. This synthetic test demonstrated that ERT is not a very useful method to explore such tiny deposits. Considering balancing the measuring speed, resolution,

and polarization effect, we cannot use a very small electrode spacing in the field work. However, the conductivity distribution from the ERT is very important, as we mentioned earlier, and the inverted conductivity distribution will be used in the next step in inverting SP and IP data.

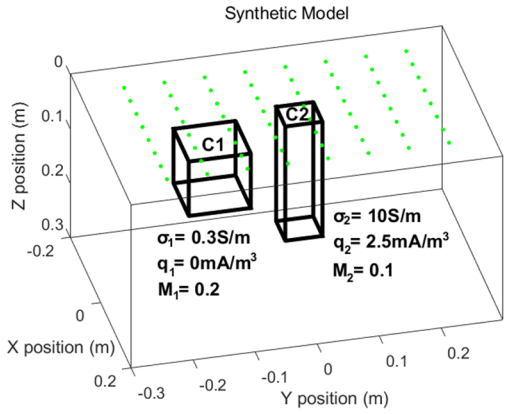

Figure 2. The 3D synthetic model. Green dots denote the position of the electrode. The area encapsulated by the black box denotes the position of the anomaly.

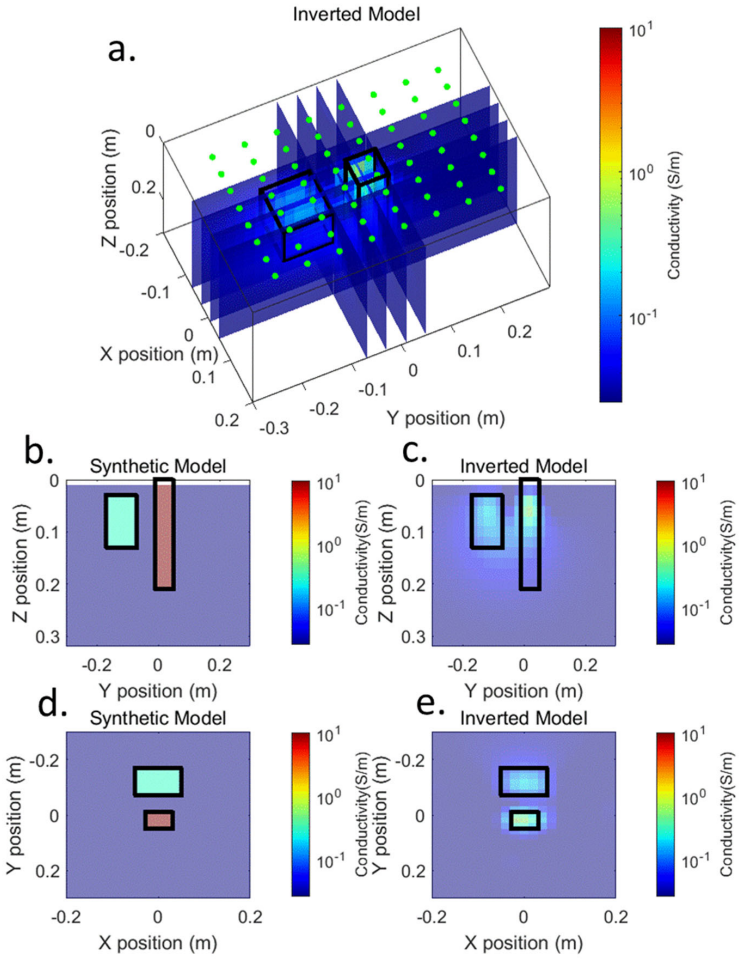

Figure 3. True and inverted conductivity distribution. (**a**) The inverted 3D conductivity distribution, (**b**) true 2D conductivity distribution cross section at x = 0 m, (**c**) the inverted 2D conductivity cross section at x = 0 m, (**d**) the true 2D conductivity cross section at z = 0.06 m, (**e**) the inverted 2D conductivity cross section at z = 0.06 m. The green dots denote the position of the electrodes. The areas encapsulated by the black boxes denote the true positions of the anomalies.

3.2. IP Inversion

For IP inversion, we use the same mesh as that used in ERT. The maximum iteration is set to 5, and the result is shown in Figure 4 after reaching the maximum iteration. Notably, the IP inversion result is better than ERT, and we were able to clearly see the anomaly C1 from the inverted 3D chargeability distribution, but the anomaly C2 is not well identified in the result. One reason is the size of C2 is small, and the other reason is the depth of investigation in the IP survey. At the same time, the chargeability of C2 is low.

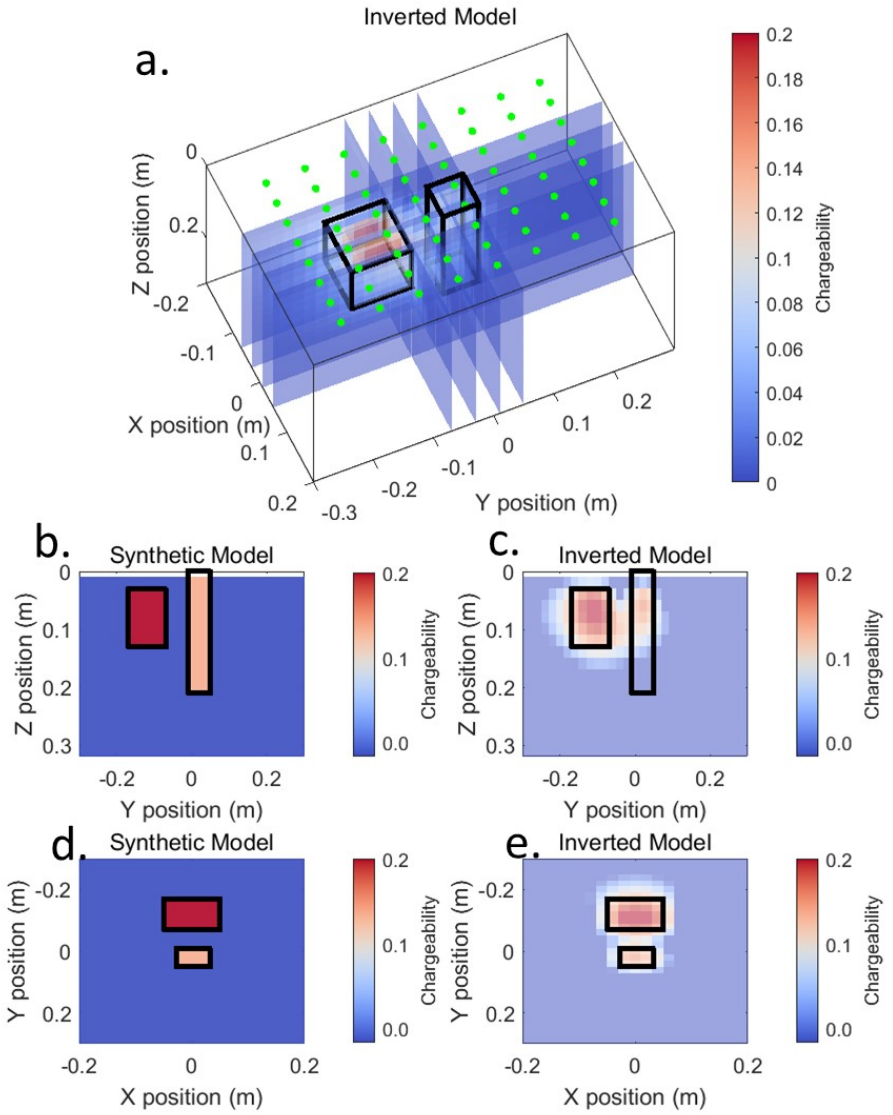

Figure 4. True and inverted chargeability distributions. (**a**) Inverted 3D chargeability distribution, (**b**) the true 2D chargeability cross section at $x = 0$ m. (**c**) Inverted 2D chargeability cross section at $x = 0$ m, (**d**) the true 2D chargeability cross section at $z = 0.06$ m. (**e**) Inverted 2D chargeability cross section at $z = 0.06$ m. The green dots denote the position of the electrodes. The areas encapsulated by the black boxes denote the true positions of the anomalies.

3.3. SP Inversion

The conductivity distribution from ERT (Figure 3) was used to calculate the kernel matrix in SP inversion, and the inverted result is shown in Figure 5. The resolution of the inverted current density in the lateral is impressive, but the bottom of anomaly C2 is not well identified. As a comparison, we use the true conductivity distribution in the SP inversion, and according to the result shown in Figure A1 in Appendix B, the resolution in the depth is improved a lot. It is crucial to emphasize the critical role of accurate

conductivity distribution in SP inversion, which underscores the importance of conducting SP surveys in conjunction with other active electromagnetic methods. The integration of inversion results from active sources for SP inversion or joint inversion of SP data with other electromagnetic data [60] truly enhances our ability to characterize ore bodies beneath the surface.

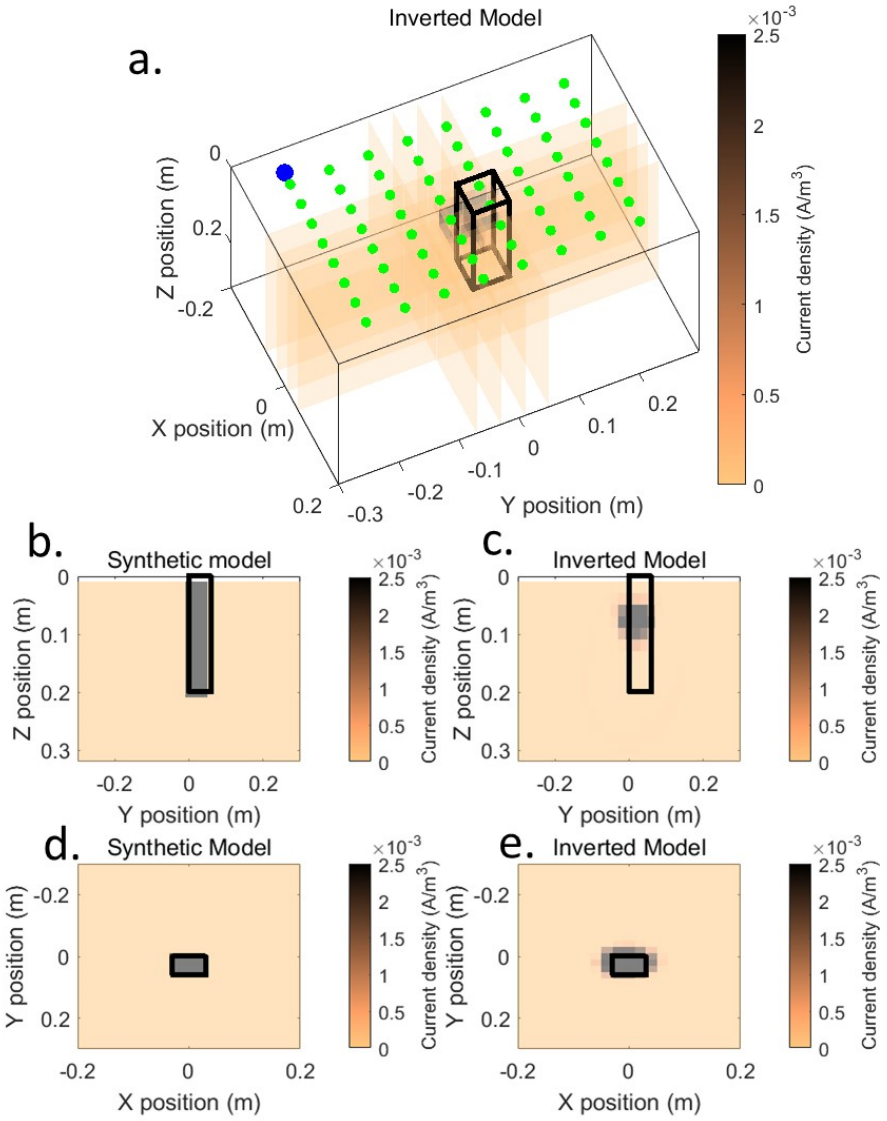

Figure 5. True and inverted current density distribution using the inverted conductivity distribution from the ERT. (**a**) The inverted 3D current density distribution, (**b**) the true 2D current density cross section at x = 0 m, (**c**) the inverted 2D current density cross section at x = 0 m, (**d**) the true 2D current density cross section at z = 0.06 m, (**e**) the inverted 2D current density cross section at z = 0.06 m. The areas encapsulated by the black boxes denote the true positions of the anomalies.

3.4. Integrated Result

We normalized the inverted chargeability and inverted source current density from IP and SP inversion and calculated the ORI χ using Equations (24) and (25). The left anomaly C1 only has the chargeability, and the anomaly C2 has low chargeability and source current density. We use $\chi > 0.5$ (which can be considered as an arbitrary threshold here) to delineate the ore bodies. The interpreted result is shown in Figure 6. Comparing the individual inversion before, the two designed anomalies were both recognized. In comparison, we also use the SP inversion result with true conductivity distribution. The new integrated result is shown in Appendix B (Figure A2). The synthetic model test

demonstrated that combining the ERT, IP, and SP data is an effective method for delineation of ore deposits. In the subsequent section, we apply the same workflow to process the sandbox data.

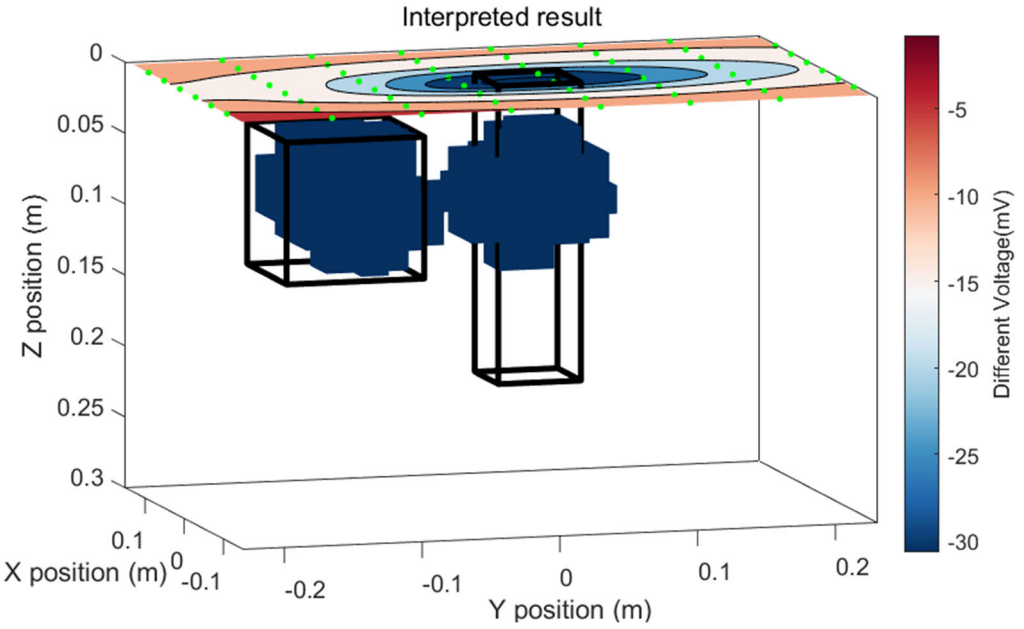

Figure 6. The interpreted result by integrating the IP data and SP data. The 2D SP anomaly is plotted on the surface. Blue cubes below the surface denote the ore bodies ($\chi > 0.5$), and the green dots denote the position of the electrodes.

4. Sandbox Experiment

4.1. Experimental Setup

The tank was filled with uniform sand. A metal bar (anomaly S1) and a pop can made of iron with liquid (anomaly S2) were placed in the sand. To accelerate the corrosion of the metal bar, the outer protective oxidation layer was removed firstly. The water used had a conductivity of 0.031 S/m at a temperature of 24.9 °C and was poured into the bottom of the box through a vertical plastic tube. The height of the water table was maintained at 14cm below the surface and was kept constant throughout the study, approximately in the middle of the metal bar and below the bottom of the pop can. Figure 7 depicts the sandbox experiment setup, including the locations of electrodes and anomalies. The tank used for this experiment had dimensions of 0.57 × 0.40 × 0.285 m. A total of 64 holes were drilling through a plastic plate in an 8 × 8 grid, and electrodes were inserted into these holes to inject current and measure voltage differences. Each hole was marked with a unique number for ER and IP investigation. The voltage difference and apparent chargeability were collected during the ERT and IP survey. Two non-polarizing $Pb/PbCl_2$ electrodes were used for the SP survey. One electrode served as the reference electrode, and the other electrode as the scanning electrode. The experiment spanned approximately two months, including ER and IP measurements and three rounds of SP measurements.

4.2. ERT

We designed a 2D protocol (the current electrodes [A B] and measuring electrodes [M N] on the same profile) for ERT data acquisition, comprising a total of 17 profiles along the x direction and y direction (Figure 7b). Along each profile, we kept the position of the injection location (electrode A) and the retrieval location (electrode B) constant, but the position of measuring electrodes M and N is changed for each measurement. This approach aims to minimize electrodes' polarization effects. The voltage difference and apparent chargeability were automatically acquired using an ABEM instrument Terrameter SAS 4000 (http://www.guidelinegeo.com, accessed on 6 November 2023), and the maximum

injection current is set to 200 mA. The injected current duration (time on) is 1 s, then the current is shut down and the partial chargeability is measured. There are a total of 237 voltage differences and partial chargeability data were recorded.

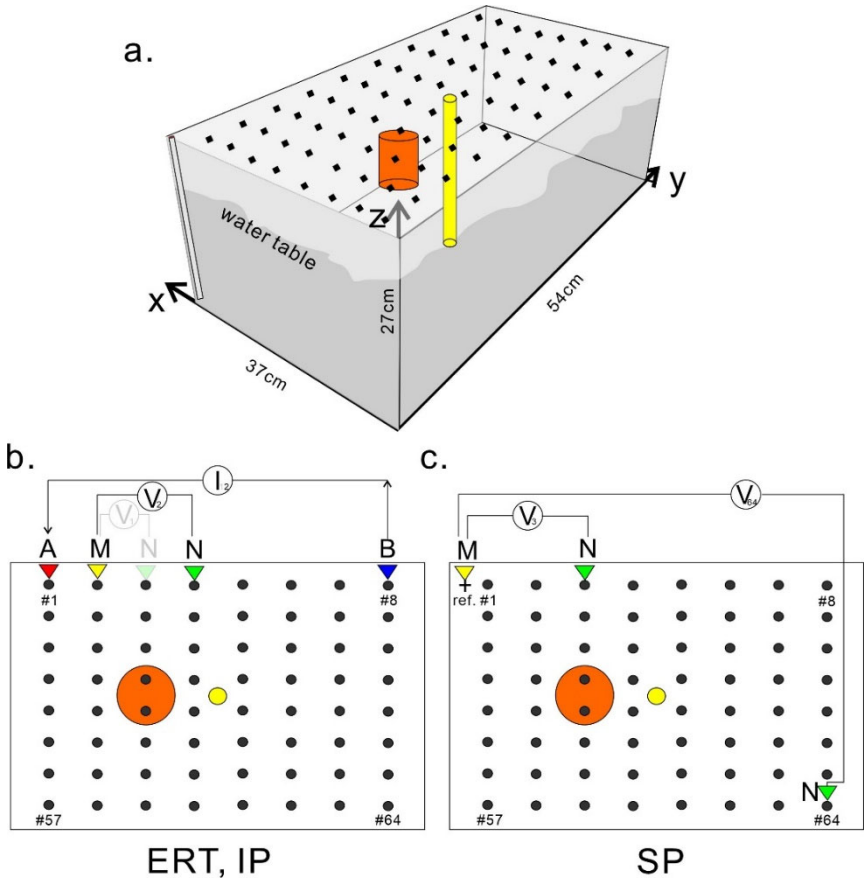

Figure 7. Experiment setup, (**a**) the diagram of the constructed tank, two anomalies are buried in the sand, the yellow one is a metal bar (anomaly S1) and the other (orange) is a pop can with liquid (anomaly S2). The black dot denotes the transmitting and measuring station. (**b**) The ER and IP survey line from the up (x/y) view, A and B denote current electrodes and M and N denotes measuring electrodes (**c**) SP survey line, ref denotes the reference electrode (M) and the Ns are the scanning electrodes.

The sandbox in Figure 7 is discretized with a $40 \times 40 \times 25$ mesh for inversion, the core mesh has a fine cell size of $0.02 \times 0.02 \times 0.02$ m. The initial value β is set to 4×10^{-3} and reduced 3 times after 2 iterations. The maximum number of iterations is set to 5. The ERT is run with a homogeneous conductivity distribution (0.025 S/m) and the reference model is the same as the start model. The inverted 3D conductivity distribution is shown in Figure 8. It seems like a homogeneous layer below the surface. The depth of investigation (DOI) in the ERT is about 0.12 m below the surface, the 2D slice $x = 0$ m and slice $z = 0.06$ m as shown in Figure 8. We could not identify the position of the buried target. The convergence is illustrated in Figure 9, and the root-mean-square (RMS) error is defined as

$$RMS = \sqrt{\frac{\phi_d(m)}{N}} \tag{26}$$

where N is the number of observed data, $\phi_d(m)$ (the first term on the right-hand side of the objective function) is the data misfit. The value of RMS is dependent upon the data-weighting matrix $\mathbf{W}_d$. As we mentioned earlier, the matrix $\mathbf{W}_d$ is often used to make sure every observed data point contributes the same weight in the objective function and also can be an identity matrix. We designed the different weight matrixes in these

inversions. $\mathbf{W}_d = diag\left(\frac{1}{\varepsilon_1}, \frac{1}{\varepsilon_2}, \cdots, \frac{1}{\varepsilon_N}\right)$ is a diagonal matrix in which ε_i stands for the standard deviation of the i_{th} data in ERT, but the identity matrix is used in the IP and SP inversion.

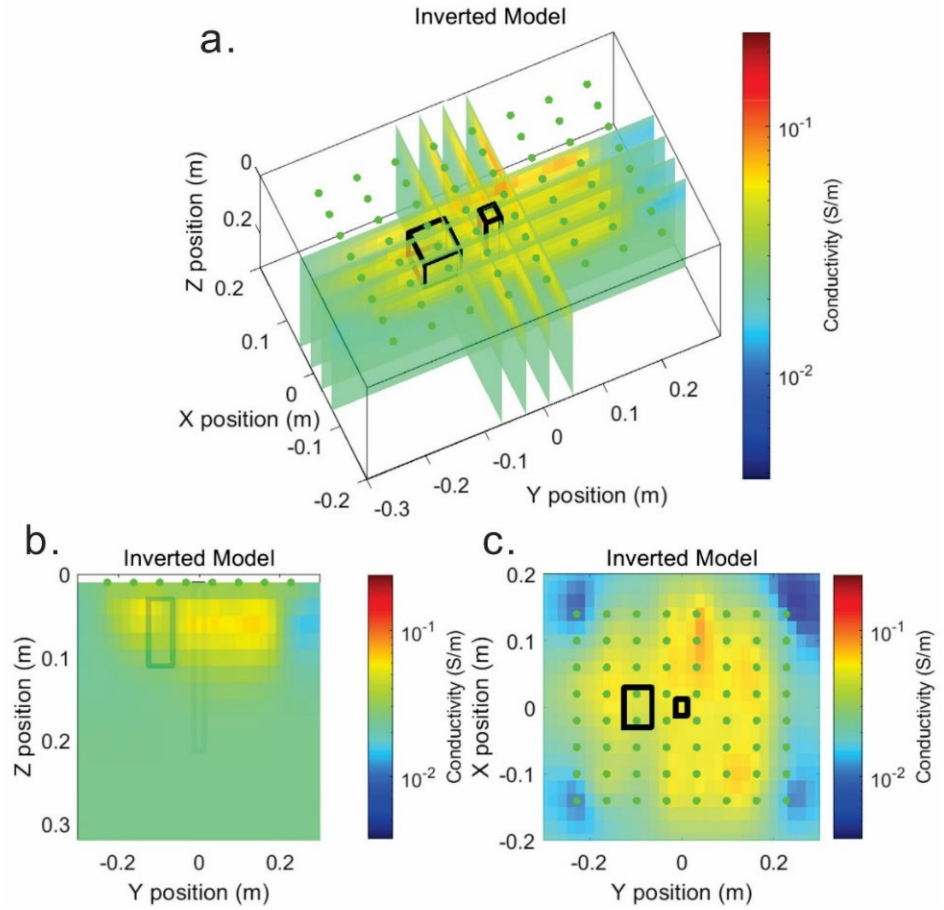

Figure 8. Inverted conductivity distribution from the ER data. (**a**) The 3D conductivity distribution, (**b**) 2D conductivity cross section at x = 0 m, (**c**) 2D conductivity cross section at z = 0.06 m. Green points denote the electrode position. The area encapsulated by the black box denotes the position of the anomaly.

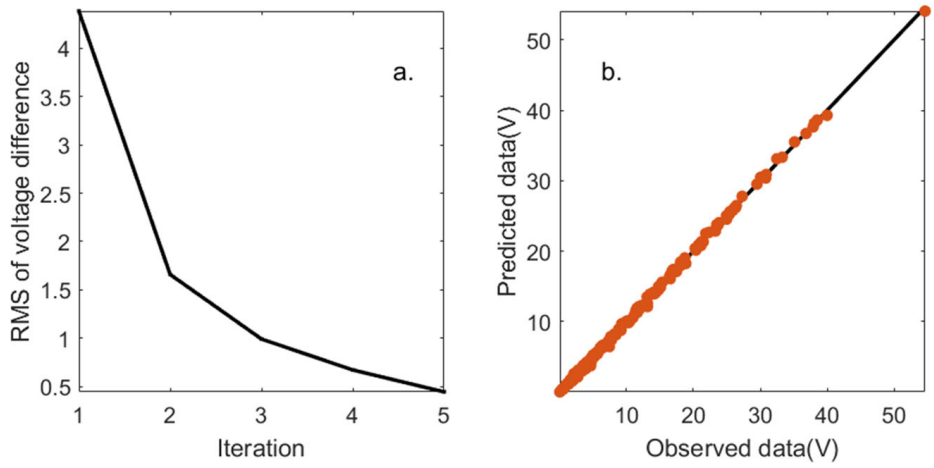

Figure 9. Convergence of the ERT and fit between the observed and predict data. (**a**) Root-mean-square (RMS) error of the voltage differences; (**b**) observed data versus the predicted data for the last iteration.

4.3. IP Inversion

After the primary current was shut down, we measured partial chargeability by integrating the secondary voltage over a time window of 0.1 s. We recorded a total of 10 partial chargeability data each time. Figure 10 illustrates the apparent chargeability decay curve over time for two different survey lines: line 1 and line 13. All survey lines share the same injection location (electrode A) and retrieval location (electrode B), but the location of measuring electrode M and electrode N is different. In survey line 1, electrode A is located at position #1 and electrode B is located at position #8. In contrast, for survey line 13, electrode A is located at position #25 and electrode B is located at position #3. As shown in Figure 7b, line 1 is located farther from the anomaly, whereas line 13 crosses the top of the anomaly. Consequently, the magnitude of the measured partial chargeability is greater in line 13 (red line in Figure 10) than line 1 (the black line in Figure 10). There are some negative chargeability values in the observed data, we treat this as noise and delete them, and the remaining data are used for IP inversion.

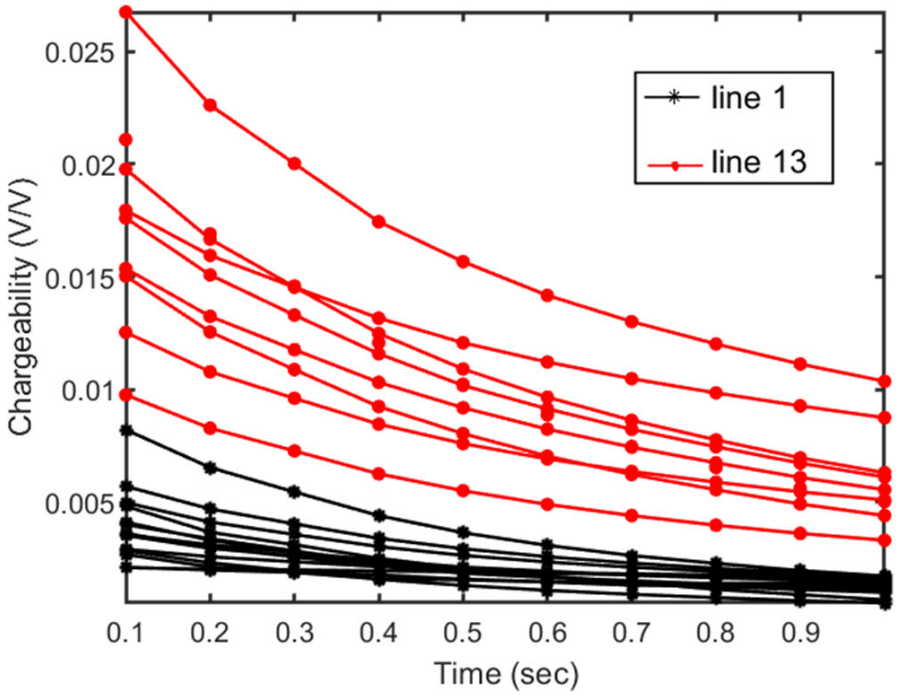

Figure 10. Apparent chargeability (in V/V) of decaying curves in different lines. Line 1 is far from the anomaly (red line), but line 13 (black line) is near the anomaly. This demonstrates that IP has a sensitivity to the presence of the metallic object located along line 13.

Traditional two-step DC-IP inversion was performed: firstly, the electrical conductivity distribution is inverted, then the chargeability distribution is inverted. Here, we use the previous inverted 3D conductivity in Figure 8 as the input and the same mesh for IP inversion. The initial value β is set to 10^{-4} and reduced 5 times after 2 iterations. The maximum number of iterations is set to 5. IP inversion is run with a homogeneous chargeability distribution (the value is 0) and no reference model cooperated in the inversion. Since the chargeability has to be positive, we add the boundary constraint in the inversion ($0 < M < 1$). Figure 11 illustrates the reconstructed 3D chargeability distribution in which we only use the apparent chargeability from the first window. We recognized the anomaly S1, but the small anomaly S2 is not recognized. Figure 12 shows that the observed data is well reproduced by the inverted chargeability.

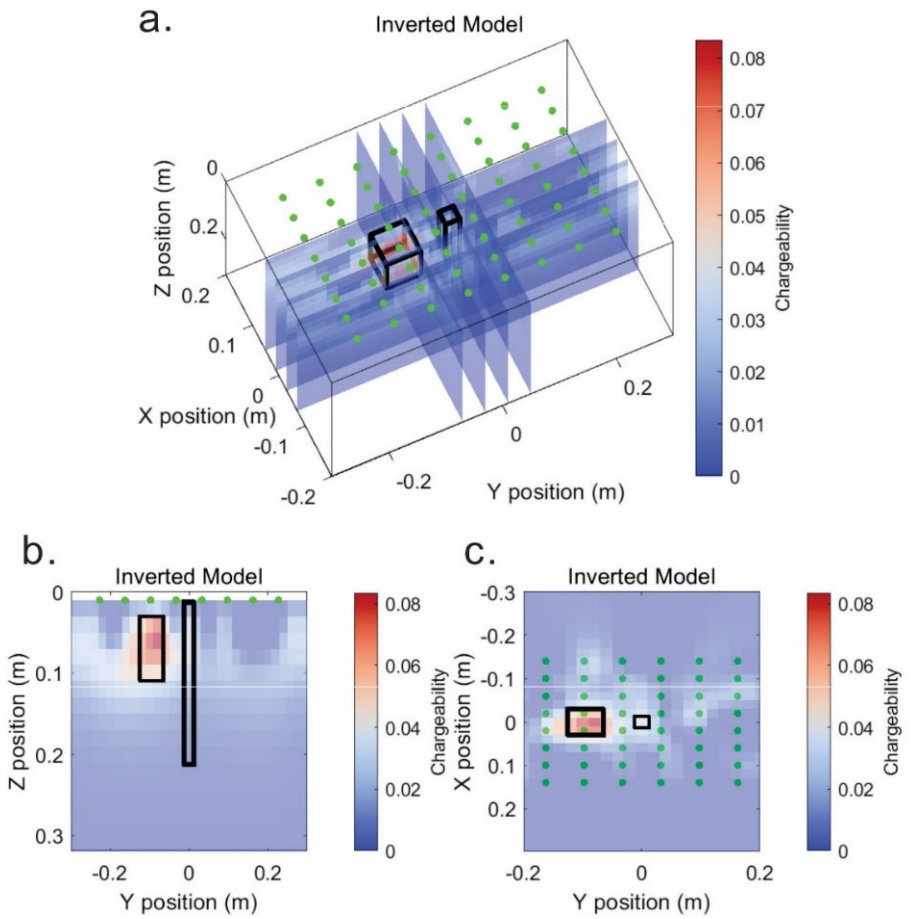

Figure 11. The inverted 3D chargeability distribution from the IP data, (**a**) 3D chargeability distribution, (**b**) 2D chargeability cross section at x = 0 m, (**c**) 2D chargeability cross section at z = 0.06 m. Green points denote the electrode position. The area encapsulated by the black box denotes the position of the anomaly.

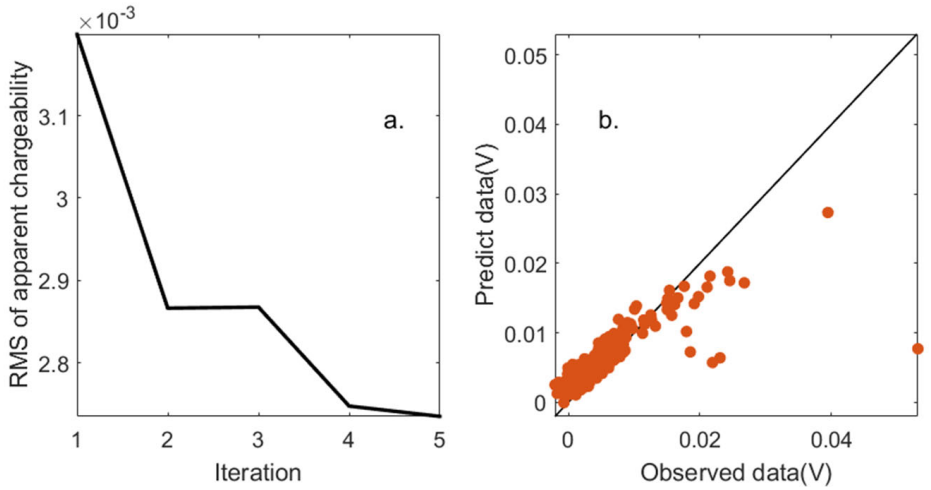

Figure 12. Convergence of the IP inversion and fit between the observed and predicted data. (**a**) Root-mean-square (RMS) error of the apparent chargeability. (**b**) Observed data versus the predicted data for the last iteration (number 5).

4.4. SP Inversion

In this experiment, SP data were acquired at the surface of the tank. Figure 13 illustrates the data collected at Day 7, Day 22, and Day 40. Initially, a total of 80 data points were collected during the first measurement (Day 7). The 64 data points for the second and third measurement used the same electrode positions as the ERT and IP (Day 22 and Day 40). The reference electrode was near location #1, and the scanning electrodes were located at #1 to #64. We should emphasize that anomaly S1 was buried at Day 18. So, we only see the SP anomaly caused by redox reaction around anomaly S2 (metal bar) near the center of the tank from the first measurement (Figure 13a), and the maximum SP anomaly reaches −70 mV, but the maximum SP is −40 mV during the second and third measurements. We attribute this difference in SP anomalies between the first two measurements to variations in electrode positions. There is no other SP anomaly during the second measurement, because the anomaly S1 was just buried and the redox action did not occur. As time goes by, the 2D distribution of SP anomalies changes (Figure 13c). Since the height of the water table is near the bottom of anomaly S2, the redox reaction of S2 is very weak.

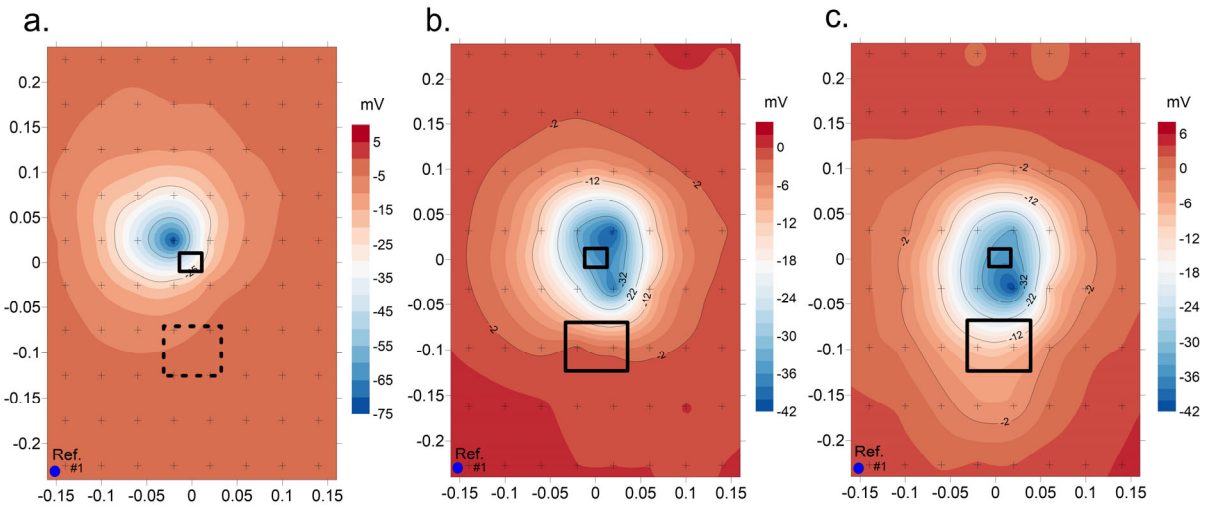

Figure 13. Development of the SP anomaly during the experiment. (**a**) The 2D self-potential anomaly at Day 7, and only anomaly S2 (the yellow one in the Figure 7a) was buried in the sand; (**b**) 2D SP anomaly at Day 22, and the secondary anomaly (the orange one in the Figure 7a) was buried at Day 18; (**c**) 2D self-potential anomaly at Day 40. Anomaly S1 is above the water table, so we think the redox action is weak. The blue dot denotes reference electrode (near electrode #1) and the crosses denote the position of scanning electrodes. The development of the anomaly over time is due to the corrosion of the metal bar. Ref denotes the references (zero potential) for the array of electrodes in the self-potential survey.

The SP anomaly at Day 22 is attributed to a redox reaction occurring around anomaly S2, and this reaction remains stable during this period. However, due to its small size, the associated chargeability is very weak. Our aim is to demonstrate the sensitivity of SP inversion in identifying such types of ore deposits. So, the SP data collected at Day 22 were used for SP inversion, and the same mesh as that used for ERT and IP inversion was used. The previous inverted 3D conductivity in Figure 8 was incorporated into the SP inversion as a priori information. The initial value β is set to 1×10^{-3}, and the threshold value α in Equation (6) is 2.2×10^{-6}. The maximum number of iterations is set to 10. SP inversion is run with a homogeneous current density (with a value of 0) and no reference model was used. Finally, the inverted 3D current density distribution showed anomaly C2 at the center of the sandbox (Figure 14). Figure 15 shows that the observed SP data is well reproduced by the inverted volumetric current source.

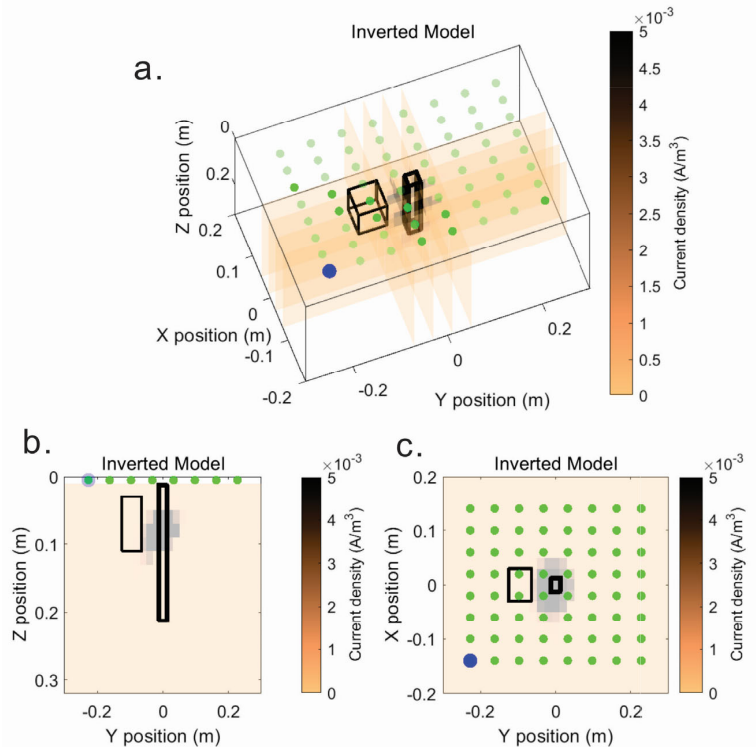

Figure 14. The inverted 3D current density distribution from the SP data. (**a**) The 3D current density distribution, (**b**) 2D current density cross section at x = 0 m, (**c**) 2D current density cross section at z = 0.06 m. The green points denote the position of the electrodes. The areas encapsulated by the black boxes denote the position of the anomalies.

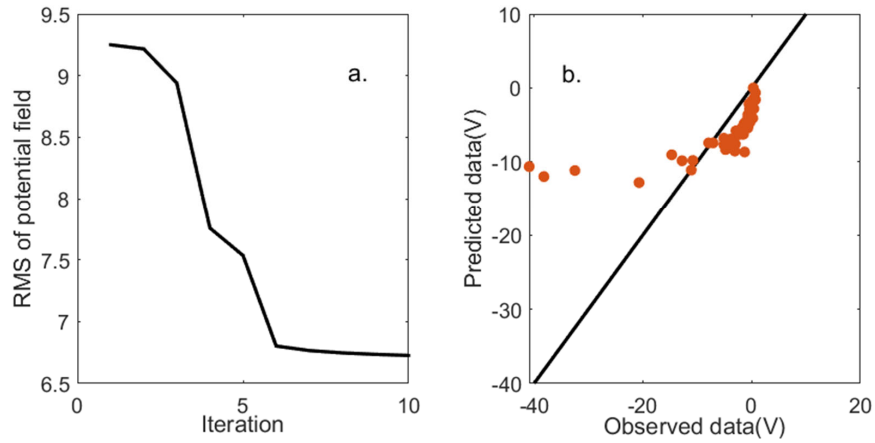

Figure 15. Convergence of the SP inversion and fit between the observed and predicted data. (**a**) Root-mean-square (RMS) error of the potential field. (**b**) Observed data versus predicted data for the last iteration.

4.5. Integrated Result

As in Section 3.4, we calculated the ORI χ and used $\chi > 0.5$ as the final interpreted result. Both anomalies were identifiable in Figure 16. The synthetic test and sandbox experiment demonstrated that combining multiple methods together enabled a more comprehensive characterization of the ore body morphology. We observed that the vertical resolution is inferior to the horizontal resolution, particularly for anomaly S2 (metal bar). Anomaly S2 was mainly reflected by inverted current density. One possible explanation is the insufficient precision of inverted conductivity. As we mentioned earlier (Equation (3)), the collected SP data are related to the conductivity distribution, and the inverted current

density relies on conductivity (see Figure A2). Another reason may be the limited depth of investigation. To obtain deep information, a larger electrode array is necessary.

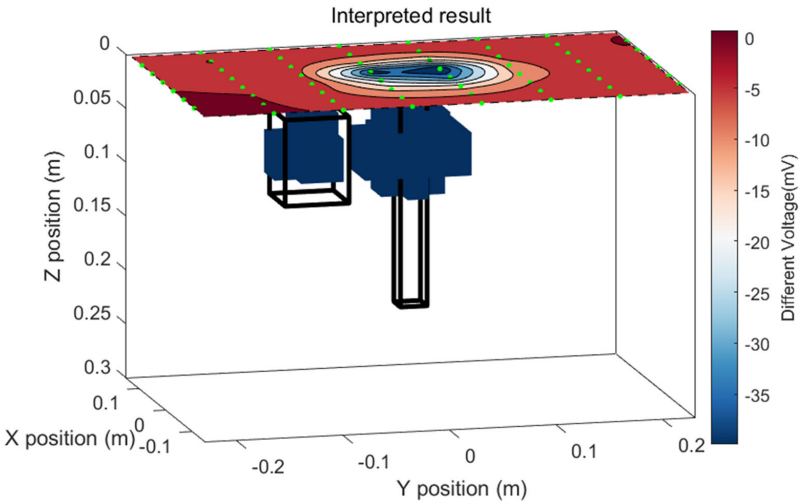

Figure 16. Interpreted result obtained by integrating the IP and SP data. The 2D-modeling SP anomaly is plotted on the surface. The blue cubes below the surface denote the ore bodies ($\chi > 0.5$), and the green dots denote the position of the electrodes.

5. Conclusions

Low-frequency geoelectrical methods offer a non-invasive and cost-efficient method for mineral exploration. However, challenges such as diminishing ore quality, increased overburden thickness, and ore body size have intensified the complexity of mineral exploration. While reducing the space of electrodes may improve the accuracy, it also increases costs, particularly in 2D/3D acquisition protocols for ER and IP surveys. SP data are sensitive to ore bodies intersecting the water table and undergoing redox reactions. However, SP inversion requires electrical conductivity, as does IP inversion. We highly recommend integrated application of ERT, IP, and SP methods in mineral exploration. In this paper, we defined an ore body index (ORI) χ using normalized inverted chargeability and current density to delineate the ore body. ORI χ tomography is sensitive to both the polarization phenomenon and redox reaction around the ore body. Compared to individual inversion, the interpreted result enhances the accuracy and feasibility of exploration of ore bodies, which are supported by synthetic models and sandbox experiments. ERT, IP, and SP data are easily collected together during the survey, and combining these data will provide critical information and insights for the exploration and development of mineral resources.

Author Contributions: Conceptualization, A.R.; Data curation, Z.S.; Formal analysis, A.G.; Investigation, Z.S., A.G., J.R., X.Z. (Xin Zhang) and X.Z. (Xiang Zhao); Methodology, Z.S., A.R., A.G., X.Z. (Xin Zhang), X.Z. (Xiang Zhao) and J.R.; Project administration, A.R.; Software, Z.S.; Supervision, A.R.; Writing—original draft, A.R. and Z.S. All authors have read and agreed to the published version of the manuscript.

Funding: This research received no external funding.

Data Availability Statement: All the data used to generate the figures associated with this manuscript have been published on GitHub (see https://github.com/ZhaoyangSU-CUP/data-for-Minerals-2023.git, accessed on 6 November 2023).

Acknowledgments: André Revil thanks the CNRS for its support over the years. Zhaoyang Su thanks the China Scholarship Council (202106440109) for its support.; Xin Zhang thanks the China Scholarship Council (202206420076) for its support. We thank three anonymous referees for their very useful reviews that have helped us to write a better manuscript.

Conflicts of Interest: The authors declare no conflict of interest.

Appendix A

The governing field equation for the self-potential problem is written as

$$\nabla \cdot (\sigma \nabla \psi) = q_v. \tag{A1}$$

Using the identity $\nabla \cdot (f\mathbf{A}) = \nabla f \cdot \mathbf{A} + f(\nabla \cdot \mathbf{A})$, Equation (A1) is written as

$$\nabla \sigma \cdot (\nabla \psi) + \sigma \nabla^2 \psi = q_v. \tag{A2}$$

From Equation (A2) and after a few algebraic manipulations, we easily obtain

$$\nabla^2 \psi = \frac{q_v}{\sigma} - \frac{\nabla \sigma}{\sigma} \cdot (\nabla \psi) \tag{A3}$$

So, we can rewrite Equation (A1) as

$$\nabla^2 \psi = \frac{q_v}{\sigma} + \nabla \ln \sigma \cdot \mathbf{E}. \tag{A4}$$

Appendix B

We use the true conductivity distribution in the SP inversion, and according to the SP inversion result shown in Figures A1 and A2, the resolution in the depth is improved a lot. However, it is not easy to obtain the exact conductivity during the survey, especially clearly distinguishing the conductivity of small anomalies from the conductivity of the surrounding rocks.

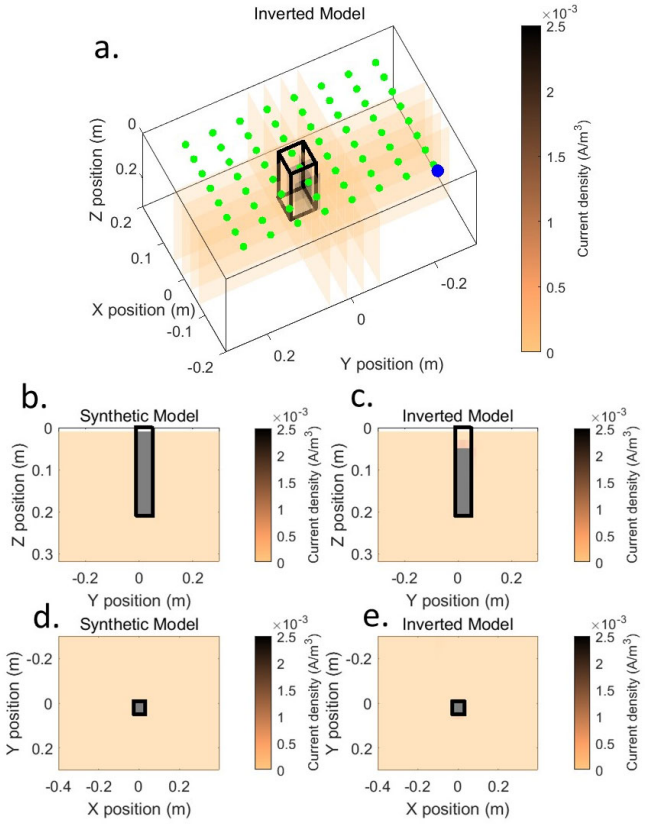

Figure A1. True and inverted current density distribution using the exact conductivity distribution from ERT. (**a**) The 3D inverted current density distribution, (**b**) the true 2D current density cross section at x = 0, (**c**) the inverted 2D current density cross section at x = 0 m, (**d**) true 2D chargeability cross section at z = 0.06 m, (**e**) the inverted 2D chargeability cross section at z = 0.06 m. The areas encapsulated by the black boxes denote the true positions of the anomalies.

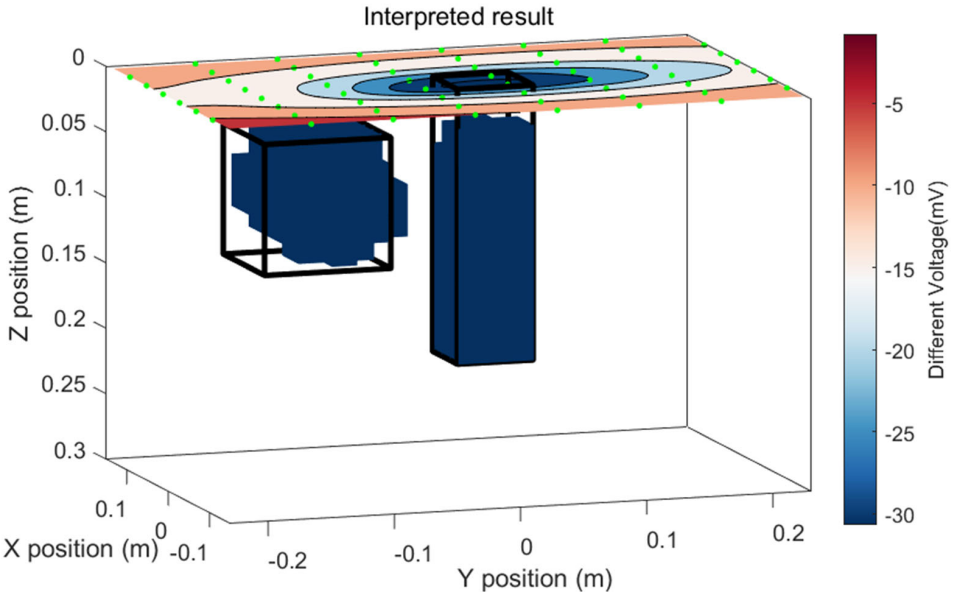

Figure A2. Final result obtained by integrating the IP data and SP data. The 2D calculated SP anomaly is on the surface. The blue cubes below the surface denote the ore bodies (OR index $\chi > 0.5$), and the green dots denote the position of the electrodes.

References

1. Okada, K. Breakthrough technologies for mineral exploration. *Miner. Econ.* **2022**, *35*, 429–454. [CrossRef]
2. Schodde, R. Recent trends in gold discovery. In Proceedings of the 2011 NewGenGold Conference, Perth, Australia, 22–23 November 2011; Volume 2, pp. 1–19.
3. Witherly, K. The evolution of minerals exploration over 60 years and the imperative to explore undercover. *Lead. Edge* **2012**, *31*, 292–295. [CrossRef]
4. Eaton, D.W.; Milkereit, B.; Salisbury, M. Seismic methods for deep mineral exploration: Mature technologies adapted to new targets. *Lead. Edge* **2003**, *22*, 580–585. [CrossRef]
5. Malehmir, A.; Durrheim, R.; Bellefleur, G.; Urosevic, M.; Juhlin, C.; White, D.J.; Milkereit, B.; Campbell, G. Seismic methods in mineral exploration and mine planning: A general overview of past and present case histories and a look into the future. *Geophysics* **2012**, *77*, WC173–WC190. [CrossRef]
6. Witherly, K.; Irvine, R.; Morrison, E.B. The Geotech VTEM time domain helicopter EM system. In *SEG Technical Program Expanded Abstracts*; SEG: Denver, CO, USA, 2004; pp. 1217–1220.
7. Sorensen, K.I.; Auken, E. SkyTEM—A New High-resolution Helicopter Transient Electromagnetic System. *Explor. Geophys.* **2004**, *35*, 194–202. [CrossRef]
8. Smith, R.S.; Hodges, G.; Lemieux, J. Case histories illustrating the characteristics of the HeliGEOTEM system. *Explor. Geophys.* **2009**, *40*, 246–256. [CrossRef]
9. Konieczny, G.; Smiarowski, A.; Miles, P. Breaking through the 25/30 Hz barrier: Lowering the base frequency of the HELITEM airborne EM system. In *SEG Technical Program Expanded Abstracts*; SEG: Denver, CO, USA, 2016; pp. 2218–2222.
10. Evans, R.L. A seafloor gravity profile across the TAG Hydrothermal Mound. *Geophys. Res. Lett.* **1996**, *23*, 3447–3450. [CrossRef]
11. Dransfield, M.; Milkereit, B. Airborne Gravity Gradiometry in the Search for Mineral Deposits. In Proceedings of the Exploration 07: Fifth Decennial International Conference on Mineral Exploration, Toronto, ON, Canada, 9–12 September 2007.
12. Martinez, C.; Li, Y.; Krahenbuhl, R.; Braga, M.A. 3D inversion of airborne gravity gradiometry data in mineral exploration: A case study in the Quadrilátero Ferrífero, Brazil. *Geophysics* **2013**, *78*, B1–B11. [CrossRef]
13. Gunn, P.; Dentith, M. Magnetic responses associated with mineral deposits. *J. Aust. Geol. Geophys.* **1997**, *17*, 145–158.
14. Nabighian, M.N.; Grauch, V.J.S.; Hansen, R.O.; LaFehr, T.R.; Li, Y.; Peirce, J.W.; Phillips, J.D.; Ruder, M.E. The historical development of the magnetic method in exploration. *Geophysics* **2005**, *70*, 33ND–61ND. [CrossRef]
15. Galley, C.; Lelièvre, P.; Haroon, A.; Graber, S.; Jamieson, J.; Szitkar, F.; Yeo, I.; Farquharson, C.; Petersen, S.; Evans, R. Magnetic and Gravity Surface Geometry Inverse Modeling of the TAG Active Mound. *J. Geophys. Res. Solid Earth* **2021**, *126*, e2021JB022228. [CrossRef]
16. Harris, A.C. Exploration and Discovery of Base-and Precious-Metal Deposits in the Circum-Pacific Region—A 2010 Perspective. *Econ. Geol.* **2012**, *107*, 1073–1074. [CrossRef]
17. Loke, M.H. Electrical Imaging Surveys for Environmental and Engineering Studies, A Practical Guide to 2-D and 3-D Survey. 1999. Volume 70. Available online: https://pages.mtu.edu/~ctyoung/LOKENOTE.PDF (accessed on 15 June 2023).

18. Chambers, J.E.; Kuras, O.; Meldrum, P.I.; Ogilvy, R.D.; Hollands, J. Electrical resistivity tomography applied to geologic, hydrogeologic, and engineering investigations at a former waste-disposal site. *Geophysics* **2006**, *71*, B231–B239. [CrossRef]
19. Abu Rajab, J.S.; El-Naqa, A.R. Mapping groundwater salinization using transient electromagnetic and direct current resistivity methods in Azraq Basin, Jordan. *Geophysics* **2013**, *78*, B89–B101. [CrossRef]
20. Zhang, G.; Zhang, G.-B.; Chen, C.-C.; Jia, Z.-Y. Research on Inversion Resolution for ERT Data and Applications for Mineral Exploration. *Terr. Atmos. Ocean* **2015**, *26*, 515–526. [CrossRef]
21. Schoor, M.V. The application of in-mine electrical resistance tomography (ERT) for mapping potholes and other disruptive features ahead of mining. *J. S. Afr. Inst. Min. Metall.* **2005**, *105*, 447–451.
22. Giao, P.; Chung, S.; Kim, D.; Tanaka, H. Electric imaging and laboratory resistivity testing for geotechnical investigation of Pusan clay deposits. *J. Appl. Geophys.* **2003**, *52*, 157–175. [CrossRef]
23. Perrone, A.; Lapenna, V.; Piscitelli, S. Electrical resistivity tomography technique for landslide investigation: A review. *Earth-Sci. Rev.* **2014**, *135*, 65–82. [CrossRef]
24. Goto, T.N.; Takekawa, J.; Mikada, H.; Kasaya, T.; Machiyama, H.; Iijima, K.; Sayanagi, K. Resistivity survey of seafloor massive sulfide areas in the Iheya north area, off Okinawa, Japan. In Proceedings of the 11th SEGJ International Symposium, Yokohama, Japan, 18–21 November 2013; pp. 298–301.
25. Park, J.-O.; You, Y.-J.; Kim, H.J. Electrical resistivity surveys for gold-bearing veins in the Yongjang mine, Korea. *J. Geophys. Eng.* **2009**, *6*, 73–81. [CrossRef]
26. Batista-Rodríguez, J.A.; Pérez-Flores, M.A. Contribution of ERT on the Study of Ag-Pb-Zn, Fluorite, and Barite Deposits in Northeast Mexico. *Minerals* **2021**, *11*, 249. [CrossRef]
27. Ishizu, K.; Goto, T.; Ohta, Y.; Kasaya, T.; Iwamoto, H.; Vachiratienchai, C.; Siripunvaraporn, W.; Tsuji, T.; Kumagai, H.; Koike, K. Internal structure of a seafloor massive sulfide deposit by electrical resistivity tomography, Okinawa Trough. *Geophys. Res. Lett.* **2019**, *46*, 11025–11034. [CrossRef]
28. Revil, A.; Florsch, N.; Mao, D. Induced polarization response of porous media with metallic particles—Part 1: A theory for disseminated semiconductors. *Geophysics* **2015**, *80*, D525–D538. [CrossRef]
29. Revil, A.; Abdel Aal, G.Z.; Atekwana, E.A.; Mao, D.; Florsch, N. Induced polarization response of porous media with metallic particles—Part 2: Comparison with a broad database of experimental data. *Geophysics* **2015**, *80*, D539–D552. [CrossRef]
30. Mao, D.; Revil, A. Induced polarization response of porous media with metallic particles—Part 3: A new approach to time-domain induced polarization tomography. *Geophysics* **2016**, *81*, D345–D357. [CrossRef]
31. Mao, D.; Revil, A.; Hinton, J. Induced polarization response of porous media with metallic particles—Part 4: Detection of metallic and nonmetallic targets in time-domain induced polarization tomography. *Geophysics* **2016**, *81*, D359–D375. [CrossRef]
32. Schlumberger, C. *Etude sur la Prospection Electrique du Sous-Sol.*; Gauthier-Villars: Paris, France, 1920.
33. Revil, A.; Vaudelet, P.; Su, Z.; Chen, R. Induced Polarization as a Tool to Assess Mineral Deposits: A Review. *Minerals* **2022**, *12*, 571. [CrossRef]
34. Hallof, P.; Yamashita, M.; Fink, J.; Sternburg, B.; McAlister, E.; Wieduwilt, W. The use of the IP method to locate gold-bearing sulfide mineralization. In *Induced Polarization Applications and Case Histories*; Society of Exploration Geophysicists: Houston, TX, USA, 1990.
35. Florsch, N.; Llubes, M.; Téreygeol, F.; Ghorbani, A.; Roblet, P. Quantification of slag heap volumes and masses through the use of induced polarization: Application to the Castel-Minier site. *J. Archaeol. Sci.* **2011**, *38*, 438–451. [CrossRef]
36. Sumner, J.S. *Principles of Induced Polarization for Geophysical Exploration*; Elsevier: Amsterdam, The Netherlands, 2012.
37. Günther, T.; Martin, T. Spectral two-dimensional inversion of frequency-domain induced polarization data from a mining slag heap. *J. Appl. Geophys.* **2016**, *135*, 436–448. [CrossRef]
38. Liu, W.; Chen, R.; Cai, H.; Luo, W. Robust statistical methods for impulse noise suppressing of spread spectrum induced polarization data, with application to a mine site, Gansu province, China. *J. Appl. Geophys.* **2016**, *135*, 397–407. [CrossRef]
39. Anderson, L.A.; Keller, G.V. A study in induced polarization. *Geophysics* **1964**, *29*, 848–864. [CrossRef]
40. Revil, A.; Jardani, A. *The Self-Potential Method: Theory and Applications in Environmental Geosciences*; Cambridge University Press: Cambridge, UK, 2013.
41. Grech, R.; Cassar, T.; Muscat, J.; Camilleri, K.P.; Fabri, S.G.; Zervakis, M.; Xanthopoulos, P.; Sakkalis, V.; Vanrumste, B. Review on solving the inverse problem in EEG source analysis. *J. NeuroEng. Rehabil.* **2008**, *5*, 25. [CrossRef] [PubMed]
42. Michel, C.M.; Murray, M.M.; Lantz, G.; Gonzalez, S.; Spinelli, L.; Grave de Peralta, R. EEG source imaging. *Clin. Neurophysiol.* **2004**, *115*, 2195–2222. [CrossRef] [PubMed]
43. Britton, J.W.; Frey, L.C.; Hopp, J.L.; Korb, P.; Koubeissi, M.Z.; Lievens, W.E.; Pestana-Knight, E.M.; St Louis, E.K. *Electroencephalography (EEG): An Introductory Text and Atlas of Normal and Abnormal Findings in Adults, Children, and Infants*; American Epilepsy Society: Chicago, IL, USA, 2016.
44. Jardani, A.; Revil, A.; Bolève, A.; Dupont, J.P. Three-dimensional inversion of self-potential data used to constrain the pattern of groundwater flow in geothermal fields. *J. Geophys. Res. Solid Earth* **2008**, *113*. [CrossRef]
45. Sato, M.; Mooney, H.M. The electrochemical mechanism of sulfide self-potentials. *Geophysics* **1960**, *25*, 226–249. [CrossRef]
46. Heritiana, A.R.; Riva, R.; Ralay, R.; Boni, R. Evaluation of flake graphite ore using self-potential (SP), electrical resistivity tomography (ERT) and induced polarization (IP) methods in east coast of Madagascar. *J. Appl. Geophys.* **2019**, *169*, 134–141. [CrossRef]

47. Embeng, S.B.N.; Meying, A.; Ndougsa-Mbarga, T.; Moreira, C.A.; Amougou, O.U.O. Delineation and Quasi-3D Modeling of Gold Mineralization Using Self-Potential (SP), Electrical Resistivity Tomography (ERT), and Induced Polarization (IP) Methods in Yassa Village, Adamawa, Cameroon: A Case Study. *Pure Appl. Geophys.* **2022**, *179*, 795–815. [CrossRef]
48. Shao, P.; Shang, Y.; Hasan, M.; Yi, X.; Meng, H. Integration of ERT, IP and SP methods in hard rock engineering. *Appl. Sci.* **2021**, *11*, 10752. [CrossRef]
49. Kasaya, T.; Iwamoto, H.; Kawada, Y.; Hyakudome, T. Marine DC resistivity and self-potential survey in the hydrothermal deposit areas using multiple AUVs and ASV. *Terr. Atmos. Ocean. Sci.* **2020**, *31*, 5. [CrossRef]
50. Zhu, Z.; Tao, C.; Shen, J.; Revil, A.; Deng, X.; Liao, S.; Zhou, J.; Wang, W.; Nie, Z.; Yu, J. Self-potential tomography of a deep-sea polymetallic sulfide deposit on Southwest Indian Ridge. *J. Geophys. Res. Solid Earth* **2020**, *125*, e2020JB019738. [CrossRef]
51. Su, Z.; Tao, C.; Shen, J.; Revil, A.; Zhu, Z.; Deng, X.; Nie, Z.; Li, Q.; Liu, L.; Wu, T. 3D self-potential tomography of seafloor massive sulfide deposits using an autonomous underwater vehicle. *Geophysics* **2022**, *87*, B255–B267. [CrossRef]
52. Kawada, Y.; Kasaya, T. Marine self-potential survey for exploring seafloor hydrothermal ore deposits. *Sci. Rep.* **2017**, *7*, 13552. [CrossRef]
53. Mendonça, C.A. Forward and inverse self-potential modeling in mineral exploration. *Geophysics* **2008**, *73*, F33–F43. [CrossRef]
54. Oldenburg, D.W.; Li, Y. Inversion for applied geophysics: A tutorial. In *Near-Surface Geophysics*; Butler, D.K., Ed.; No.13 in Investigations in Geophysics; SEG: Tulsa, OK, USA, 2023; Chap 5; pp. 89–150.
55. Sill, W.R. Self-potential modeling from primary flows. *Geophysics* **1983**, *48*, 76–86. [CrossRef]
56. Rittgers, J.B.; Revil, A.; Karaoulis, M.; Mooney, M.A.; Slater, L.D.; Atekwana, E.A. Self-potential signals generated by the corrosion of buried metallic objects with application to contaminant plumes. *Geophysics* **2013**, *78*, EN65–EN82. [CrossRef]
57. Amestoy, P.R.; Duff, I.S.; L'excellent, J.-Y.; Li, X.S. Analysis and comparison of two general sparse solvers for distributed memory computers. *ACM Trans. Math. Softw.* **2001**, *27*, 388–421. [CrossRef]
58. Amestoy, P.R.; Guermouche, A.; L'Excellent, J.-Y.; Pralet, S. Hybrid scheduling for the parallel solution of linear systems. *Parallel Comput.* **2006**, *32*, 136–156. [CrossRef]
59. Revil, A.; Karaoulis, M.; Srivastava, S.; Byrdina, S. Thermoelectric self-potential and resistivity data localize the burning front of underground coal fires. *Geophysics* **2013**, *78*, B259–B273. [CrossRef]
60. Su, Z.; Tao, C.; Zhu, Z.; Revil, A.; Shen, J.; Nie, Z.; Li, Q.; Deng, X.; Zhou, J.; Liu, L. Joint Interpretation of Marine Self-Potential and Transient Electromagnetic Survey for Seafloor Massive Sulfide (SMS) Deposits: Application at TAG Hydrothermal Mound, Mid-Atlantic Ridge. *J. Geophys. Res. Solid Earth* **2022**, *127*, e2022JB024496. [CrossRef]
61. Patella, D. Self-potential global tomography including topographic effects. *Geophys. Prospect.* **1997**, *45*, 843–863. [CrossRef]
62. Minsley, B.J.; Sogade, J.; Morgan, F.D. Three-dimensional source inversion of self-potential data. *J. Geophys. Res.* **2007**, *112*. [CrossRef]
63. Hansen, P.C.; O'Leary, D.P. The Use of the L-Curve in the Regularization of Discrete Ill-Posed Problems. *SIAM J. Sci. Comput.* **1993**, *14*, 1487–1503. (In English) [CrossRef]
64. Last, B.J.; Kubik, K. Compact gravity inversion. *Geophysics* **1983**, *48*, 713–721. [CrossRef]
65. Zhdanov, M.S.; Ekaterina, T. Minimum support nonlinear parametrization in the solution of a 3D magnetotelluric inverse problem. *Inverse. Probl.* **2004**, *20*, 937. [CrossRef]
66. Pidlisecky, A.; Haber, E.; Knight, R. RESINVM3D: A 3D resistivity inversion package. *Geophysics* **2007**, *72*, H1–H10. [CrossRef]
67. Haber, E. *Computational Methods in Geophysical Electromagnetics*; Mathematics in Industry Series; Society for Industrial and Applied Mathematics: Philadelphia, PA, USA, 2014.
68. Slater, L.D.; Lesmes, D. IP interpretation in environmental investigations. *Geophysics* **2002**, *67*, 77–88. [CrossRef]
69. Florsch, N.; Llubes, M.; Téreygeol, F. Induced polarization 3D tomography of an archaeological direct reduction slag heap. *Near Surf. Geophys.* **2012**, *10*, 567–574. [CrossRef]
70. Oldenburg, D.W.; Li, Y. Inversion of induced polarization data. *Geophysics* **1994**, *59*, 1327–1341. [CrossRef]